Direct electromagnetic coupling to determine diagnostic bone fracture stiffness

Jakob G. Wolynski[1]^, Milan M. Ilić[2]^, Kevin M. Labus[1]^, Branislav M. Notaroš[3]^, Christian M. Puttlitz[1]^, Kirk C. McGilvray[1]^

[1]Orthopaedic Bioengineering Research Laboratory, Departments of Mechanical Engineering and School of Biomedical Engineering, Colorado State University, Fort Collins, Colorado, USA; [2]School of Electrical Engineering, University of Belgrade, Belgrade, Serbia; [3]Department of Electrical and Computer Engineering, Colorado State University, Fort Collins, CO, USA

Contributions: (I) Conception and design: All authors; (II) Administrative support: CM Puttlitz, KC McGilvray; (III) Provision of study materials or patients: JG Wolynski; (IV) Collection and assembly of data: JG Wolynski; (V) Data analysis and interpretation: JG Wolynski, KM Labus, CM Puttlitz, KC McGilvray; (VI) Manuscript writing: All authors; (VII) Final approval of manuscript: All authors.

Correspondence to: Kirk C. McGilvray, PhD. 1374 Campus Delivery, Fort Collins, CO 80523, USA. Email: kirk.mcgilvray@colostate.edu.

Background: Rapid prediction of adverse bone fracture healing outcome (e.g., nonunion and/or delayed union) is essential to advise adjunct therapies to reduce patient suffering and improving healing outcome. Radiographic diagnostic methods remain ineffective during early healing, resulting in average nonunion diagnosis times surpassing six months. To address this clinical deficit, we developed a novel diagnostic device to predict fracture healing outcome by noninvasive telemetric measurements of fracture bending stiffness. This study evaluated the hypothesis that our diagnostic antenna system is capable of accurately measuring temporal fracture healing stiffness, and advises the utility of this data for expedited prediction of healing outcomes during early (≤3 weeks) fracture recovery.

Methods: Fracture repair was simulated, in reverse chronology, by progressively destabilizing cadaveric ovine metatarsals (n=8) stabilized via locking plate fixation. Bending stiffness of each fracture state were predicted using a novel direct electromagnetic coupling diagnostic system, and results were compared to values from material testing (MT) methods. While direct calculation of fracture stiffness in a simplistic cadaver model is possible, comparable analysis of the innumerable permutations of fracture and treatment type is not feasible. Thus, clinical feasibility of direct electromagnetic coupling was explored by parametric finite element (FE) analyses (n=1,632 simulations). Implant mechanics were simulated throughout the course of healing for cases with variations to fracture size, implant type, implant structure, and implant material.

Results: For all fracture states, stiffness values predicted by the direct electromagnetic coupling system were not significantly different than those quantified by *in vitro* MT methods [P=0.587, P=0.985, P=0.975; for comparing intact, destabilized, and fully fractured (FF) states; respectively]. In comparable models, the total implant deflection reduction (from FF to intact states) was less than 10% different between direct electromagnetic coupling measurements (82.2 µm) and FE predictions (74.7 µm). For all treatment parameters, FE analyses predicted nonlinear reduction in bending induced implant midspan deflections for increasing callus stiffness.

Conclusions: This technology demonstrates potential as a noninvasive clinical tool to accurately quantify healing fracture stiffness to augment and expedite healing outcome predictions made using radiographic imaging.

Keywords: Fracture healing; fracture stiffness; bone; nonunion; diagnostic

---

^ ORCID: Jakob G. Wolynski, 0000-0003-2659-337X; Milan M. Ilić, 0000-0003-4196-3594; Kevin M. Labus, 0000-0003-2072-6565; Branislav M. Notaroš, 0000-0002-5755-961X; Christian M. Puttlitz, 0000-0002-1255-8867; Kirk C. McGilvray, 0000-0003-1302-9307.

Introduction

Failed bone fracture healing (nonunion and/or delayed unions) is exceedingly detrimental to patients, resulting in chronic pain, need for additional surgical intervention, increased prescription opioid usage, and a reported 118% increase in treatment costs (1,2). Despite ongoing advances in orthopaedic fracture fixation techniques, nonunion incidences remain prevalent, especially among long bones such as the tibia, where up to 12% of cases experience nonunion (1). For these cases, it is clear that rapid diagnosis of adverse fracture healing is paramount for advising adjunct therapies during the early phases of healing to minimize suffering and financial burden to the patient (3,4).

Bone fracture healing is characterized by a complex cascade of overlapping phases of inflammation, repair, and remodeling (5); the exact course of fracture healing is highly influenced by the biomechanical (6) and biological environment at the fracture site (7,8). Infection, insufficient biological activity, and/or suboptimal mechanical fixation can all lead to cessation of healing progression (9), with the majority of nonunion causes being multi-factorial (10). *A priori* prediction of nonunion proves exceedingly difficult due to the numerous treatment and patient specific factors contributing to nonunion (11-13). Clinical distinction of nonunions from delayed unions (i.e., fractures which will properly heal, albeit slowly) makes diagnosis of nonunion an especially arduous task.

Planar X-ray imaging is the prevailing fracture healing diagnostic tool; however, this technology has proven to be limited by clinician interpretation (14-17). These inherent limitations limit the reliability of radiographic predictions of healing outcome (18) and delay the mean nonunion diagnosis time to 6.2 months (19).

Fracture bending stiffness has exhibited efficacy as a reliable (20-25) and early predictor (26,27) of healing outcome. Regrettably, X-ray data have been shown to be an inadequate predictor of fracture stiffness (17). Accordingly, it is common clinical practice to augment radiographic data with semi-quantitative mechanical assessments of the fracture's stability, as determined through manual manipulation of the fracture site. These methods, however, have demonstrated insufficient accuracy in correctly predicting fracture stiffness (28).

To this end, efforts have been made to develop technologies to accurately quantify the progression of fracture biomechanics throughout the healing cascade (23,29). The underlying principle of these technologies results from bone segments stabilized by orthopaedic hardware behaving as a composite structure. As proper healing progresses, structural and compositional evolution of the fracture callus leads to resultant improvements in the mechanical stiffness of the fracture site. Stiffness of the bone-callus-hardware composite is accordingly increased (23), and the share of mechanical load supported by the fixation hardware is shifted to the healing callus tissues (30). Proper healing is indicated by the progressive increase in stiffness of the composite structure, while adverse healing presents a temporally invariant stiffness (31). It has been observed that these temporal biomechanical profiles present prior to the callus mineralization required for radiographic indicators of healing. Thus, quantitative mechanical diagnostic approaches which do not rely upon radiographic methods have exhibited success as an objective and temporally expedited predictor of fracture healing outcome (26,32).

Mechanical diagnostic technologies have predominately targeted fractures treated via external fixation approaches due to the ease in instrumenting externally located fixation hardware for mechanical analyses (21,26,27,33-37). Such methods preclude application to orthopaedic fixation plates and intramedullary nails (IMN), despite their clinical ubiquity. Extensive studies have been performed to develop implantable telemetric sensors capable of measuring the mechanical state of the implant hardware and wirelessly reporting these values to external data acquisition devices (31,32,38-54). These devices must surmount extensive engineering design challenges associated with powering and interrogating sensors through biological tissues, and often require implant hardware geometry to be modified to accommodate sensor architecture (32,38,39) which increases the barriers to clinical implementation and can lead to premature/catastrophic implant failure (40).

To mitigate these limitations, our research group has developed direct electromagnetic coupling antenna (DEC) systems which non-invasively quantify relative changes in bending stiffness of fractures stabilized by any clinically

available metallic implant [i.e., IMN or plate; titanium (Ti) or stainless steel (SS)]. DEC is comprised of an antenna designed to couple with metal implants in its near-field to produce an apparent resonant frequency (ARF) which varies according to the distance between the coupled members (55). Application of controlled mechanical loads, such as four-point bending, produces changes in implant displacement (i.e., deflections) of magnitude dependent upon fracture stiffness (56,57). Implant deflections, per applied bending load, are measured via change in antenna ARF (ARF shifts) to non-invasively quantify relative fracture stiffness. Similar to the previously discussed technologies, DEC is hypothesized to provide an early and objective prediction of fractures trending towards nonunion by elucidating cases which exhibit temporal fracture stiffness invariance prior to the presentation of radiopaque tissues.

Coiled coaxial DEC antennas have demonstrated efficacy in quantifying relative changes in fracture stiffness in cadaveric (56) and *in vivo* fracture models (57). However, the original DEC antenna design was limited by reduced antenna sensitivity and a large antenna size. Accordingly, a novel Vivaldi style DEC antenna was designed to minimize antenna size while increasing DEC sensitivity to SS and Ti implant deflections (58). New antenna calibration methods were developed in this study to enable antenna sensitivity (i.e., ARF shift per applied load) to be converted directly to fracture stiffness, as the latter metric is more clinically relevant.

We hypothesized this new DEC antenna design, and associated antenna calibration methods, would enable accurate non-invasive quantification of fracture stiffness. One purpose of this study is to evaluate the accuracy of fracture stiffness values predicted by this DEC diagnostic technique by comparing with values obtained by traditional material testing (MT) methods in an ovine cadaveric fracture model.

Of additional interest are the deflections of orthopaedic implants during mechanical loading of fractured limbs, as this is foundational to the applicability of DEC as a predictor of healing outcome. These deflections are specific to the mode and magnitude of applied mechanical load, and ostensibly vary with fracture type and fixation implant selection. These highly specific factors preclude the use of existing literature to predict temporal changes in implant deflections, and exhaustive *in vivo* tests of the myriad combinations of fracture and treatment type are neither feasible nor ethical. Yet, this data is imperative for predicting the efficacy of DEC as a diagnostic tool for a variety of clinically relevant cases.

This knowledge gap can be addressed through the use of finite element (FE) analysis, which enables *in silico* simulation of bone-implant constructs during mechanical loading. FE methods additionally permit the fracture geometry, state of healing, and implant type to be rapidly and parametrically varied to evaluate implant deflections under innumerable circumstances of clinical relevance. FE and numerical analyses have frequently been implemented in fracture healing studies to evaluate the effects of implant design (59-62), implant placement (63-65), bone-implant load transfer (66-68), screw placement configurations (62,65,69), fracture geometry (65,70-74), and the mechanoregulation of healing (70,75-79). Yet to the authors' knowledge, only one prior study has implemented this technique to predict implant deflections (56), and this study was limited to a singular variation of fracture-treatment type. Thus, an additional goal of this study was to conduct a parametric series of 1,632 FE analyses to better characterize implant deflections. These data quantify the potential sensitivity for this new DEC system for a variety of permutations in fracture stabilization approach and fracture callus mechanical stability. Taken together, these data will have identified the efficacy and optimal applications for this new DEC system. We present the following article in accordance with the ARRIVE reporting checklist (available at https://atm.amegroups.com/article/view/10.21037/atm-21-5315/rc).

Methods

Ex vivo prediction of fracture stiffness

Fracture stiffness prediction by DEC diagnostic device
To better understand the potential of the DEC system as a diagnostic tool, it was necessary to test the accuracy of its predicted fracture stiffness values relative to standard *in vitro* methods (*Figure 1A-1E*). Healthy cadaveric ovine metatarsals (Rambouillet cross, female, >3 years of age, n=8) were obtained from animals sacrificed from unrelated studies. Sheep were selected for this study due their orthopaedic similarities to humans; namely, their similarity in body weight, bone macrostructure (80), cortical microarchitecture, and bone mineral composition (81). A skin incision was made along the lateral midspan of the samples so that a nine-hole SS locking compression plate (LCP; VP4045.09; DePuy Synthes; Warsaw, IN, USA) could be fixed to the bone via standard surgical practice. The LCP was secured to the mid-diaphysis with eight

Page 4 of 16

Wolynski et al. Healing bone fracture stiffness measured by diagnostic DEC

bicortical locking screws (3.5 mm diameter, 316 L SS). The middle screw hole was filled with a locking screw head (i.e., screw threads removed leaving only the locking head) to facilitate subsequent ostectomy at the LCP midspan and to maintain consistent methods to prior analogous tests (57) (*Figure 1A*). Overlaying soft tissue was restored using standard suturing techniques.

Samples were placed in a custom pneumatic DEC loading fixture that controlled four-point bending loads applied to the sample, thus inducing implant deflections towards the DEC antenna positioned at the LCP midspan (*Figure 1B*) (57). The DEC antenna was affixed to a precision linear actuator to enable the initial sample-antenna distance to be approximately 0.5 mm. Bending moment was produced by increasing the compressive force applied to the inner bending points, with resultant load cell measurements (Model 53; Honeywell; Charlotte, NC, USA) being converted to maximum bending moment based on four-point bending fixture geometry. Antenna ARF was measured via vector network analyzer (VNA) (TTR500; Tektronix; Beaverton, OR; Reflection coefficient measured from 1,550–1,850 MHz at 500 equally spaced points, 7 dBm power) (*Figure 1C*).

Bending loads were applied to the intact sample (1.0–2.5 N-m, in 0.25 N-m increments, n=5 preload cycles, and n=5 data collection cycles per test, *Figure 1B-1D*) while measuring the resultant change in ARF shift (*Figure 2A*) (57). Following loading cycles, an antenna calibration procedure was performed in which the antenna was displaced with a linear actuator while measuring resultant changes in ARF (–0.05 to +0.05 mm relative to antenna position during bending measurements, 0.01 mm step sizes, n=7 data points per position, n=5 displacement cycles per data collection). Slope of a linear fit applied to the calibration data was used to determine the expected ARF shift per change in antenna-implant distance (calibration factor, in units of ΔMHz/Δmm) for the current testing configuration (*Figure 2B*). ARF shifts from the preceding DEC bending tests were divided by this calibration factor to obtain predictions of implant displacements. Fracture stiffness was then calculated from the slope of a linear fit applied to the resultant DEC bending moment-displacement data (*Figure 2C*).

Fracture stiffness quantification via MT methods
Following DEC methods, fracture stiffness was quantified using traditional MT techniques. Samples were transferred to a servo-hydraulic MT machine (Landmark 370.02; MTS Systems Corp., Eden Prairie, MN, USA) equipped with

a four-point bending fixture of comparable mechanical configuration to the DEC loading device (*Figure 1E*). Cyclic four-point bending loads were applied to the sample via compressive displacement of the MT machine crosshead (1.0–3.0 N-m at 0.05 mm/s cross-head displacement rate, n=5 preconditioning load cycles, and n=5 data collection cycles per test). Fracture bending stiffness was calculated from the slope of a linear fit applied to the moment-cross head displacement data.

After MT stiffness had been determined, destabilized (DS) and fully fractured (FF) states were created via bone saw ostectomy trans to the LCP midspan (56,57). DS states were characterized by removal of all but half of the cortex adjacent to the LCP; FF states were characterized by removal of the remaining cortex (i.e., cutting the bone into separate proximal and distal halves, *Figure 1A*). DEC and MT quantifications of bending stiffness were performed for each sample, in all fracture states, using the aforementioned methods.

Study design
The progressive fracture destabilization technique precluded blinded testing and randomized treatment/ fracture state, but the order of DEC and MT tests of each fracture state were randomly decided by random number generation. Sample size was determined *a priori* according to a previous study where statistically significant differences in DEC measurements of *ex vivo* simulated fracture state (i.e., using a cadaveric fracture model identical to this study), and in postmortem MT measurements of ovine fracture bending stiffness, were apparent using an identical sample size (n=8) (57). In the current study, pre-sacrifice inter-specimen animal confounders were not thought to be substantive for a comparative cadaveric *ex vivo* study, and thus were not controlled. Ethical committee approval was not required due to samples being retrieved from animals sacrificed for unrelated purposes. A singular exclusion criterion was implemented such that selected cadaveric samples featured healthy metatarsals of sufficient length to accommodate the LCP geometry. No data was omitted from when comparing MT and DEC stiffness values. Single outliers were removed from the DS and FF groups when calculating individual sample's percent differences between MT and DEC predicted bending stiffness values.

Statistical analysis
Following statistical tests of equal variance, fracture bending stiffness values for each technique and fracture
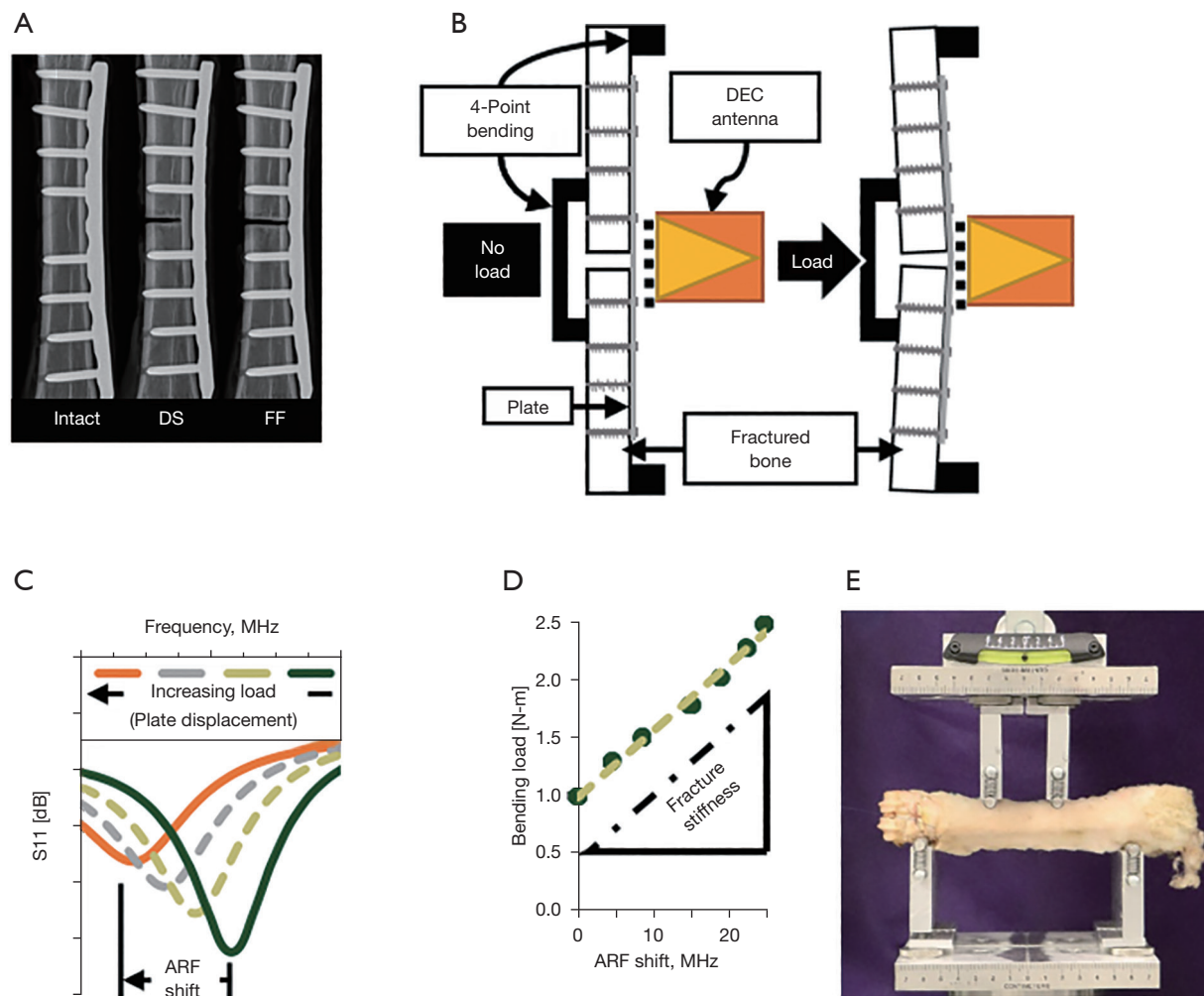
Figure 1 Direct electromagnetic coupling (DEC) fracture stiffness prediction methods. (A) Radiographic images showing samples in an intact, destabilized (DS), and fully fractured (FF) state. (B) Schematic representation of the custom DEC four-point bending device used. Application of bending loads cause the implant hardware to deflect towards the DEC antenna. (C) The resultant implant deflections cause antenna resonant frequency (ARF) to shift in a predictable and measurable manner. (D) The slope of the resultant load-ARF shift data was combined with calibration data to predict fracture stiffness. (E) DEC predictions of fracture stiffness were compared with stiffness measurements obtained using standard *in vitro* four-point bending protocols.

state were statistically compared using a two-way repeated measures analysis of variance (ANOVA) with *post-hoc* Tukey Test ($\alpha=0.05$, Minitab 18; Minitab LLC; State College, PA, USA).

FE predictions of implant deflections

Model generation
While direct calculation of fracture stiffness in a relatively simplistic cadaveric model is possible using the methods of the previous section, comparable analysis of the innumerable permutations of fracture and treatment type, over the continuous stages of healing (i.e., the gradient in elastic modulus of the callus during healing), is not feasible using *in vivo* or *ex vivo* models. Yet these data are vital to inform the DEC approach; specifically, these data can validate the foundational hypothesis that for all fracture and treatment types, healing induced changes to callus stiffness result in quantifiable reduction in implant bending deflections. To this end, 1,632 FE analyses were performed
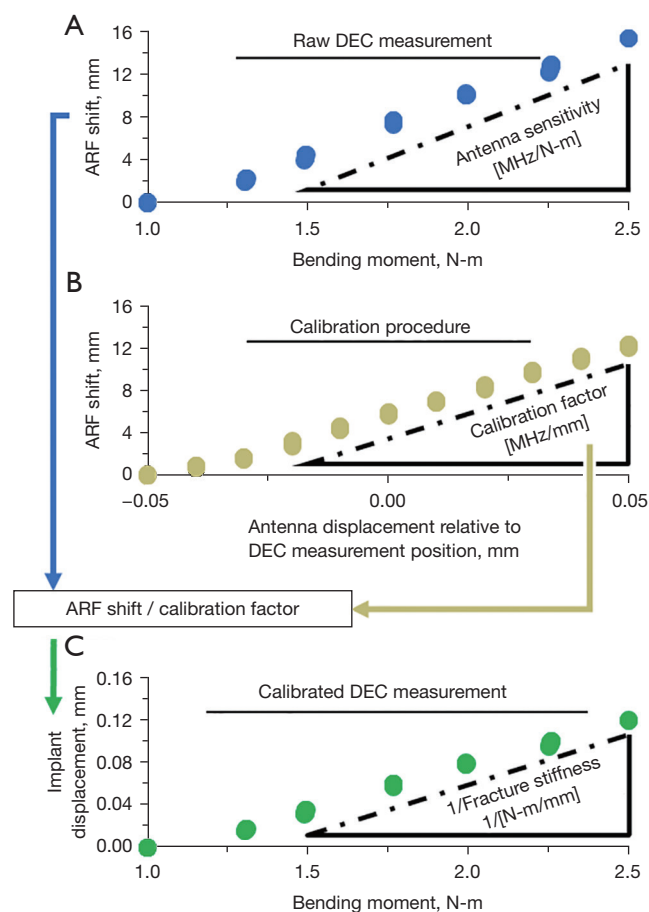
Figure 2 Methods for converting direct electromagnetic coupling (DEC) measurements into fracture stiffness. (A) Change in apparent resonant frequency (ARF shift) is measured by the DEC antenna during four-point bending of the fracture site (*Figure 1*). (B) Immediately after performing DEC bending measurements, the DEC antenna is displaced relative to the fractured limb, via precision linear actuator, to determine ARF shift for a known change in implant-antenna distance. Antenna calibration factor is obtained from the slope of a linear fit applied to the resultant ARF shift-antenna displacement data. (C) ARF shifts from the DEC bending experiment (A) are converted to implant displacements by dividing by the calibration factor. Fracture bending stiffness is obtained from the inverse of the slope of a linear slope fitted to the resultant implant displacement-bending moment data.

to predict implant deflections for parametric variations of fracture elastic modulus (n=17), fracture types (n=8), implant treatment type (n=2), implant structure (n=3), and implant material (n=2).

CT images of a healthy ovine metatarsal (*Figure 3A*)

were segmented using open source medical image processing software (ITK-SNAP, Version 3.8.0) (82) to produce a surface mesh of the bone geometry. This was then converted to a three-dimensional part file to make geometric modifications (*Figure 3B*) corresponding to fracture and treatment type (SOLIDWORKS 2018 SP5.0; Dassault Systèmes; Vélizy-Villacoublay, France). Three-dimensional part files were also generated for a LCP and locking screws of equivalent geometry to those used in the prior cadaveric study, and for an IMN (7 mm diameter, 147 mm length, two 3.5-mm pins for securing the proximal and distal ends). The LCP geometry was modeled to follow the lateral contours of the metatarsal geometry, similar to what would be used in a clinical environment (*Figure 3C*).

Additional models were generated for LCP and IMN with approximately 50% increased and 50% decreased structural stiffness based upon changes in their cross-sectional geometry (i.e., +/−50% of original sections' second moment of area in the direction of applied bending). LCP were thus modeled with a thickness of 3.57, 4.50, or 5.15 mm; IMN were modeled with a diameter of 5.88, 7.00, or 7.75 mm. The metatarsal geometry required modification to accommodate the different types of hardware fixation: three models were created with intramedullary reaming for the corresponding IMN sizes, and a single model was created for the LCP models. To analyze the effect of osteotomy fracture size, separate geometric models were created featuring mid-diaphyseal fractures with non-reduced fracture gaps varying from one to eight mm, in one mm increments. A 1.0 index fracture callus (i.e., no periosteal callus) was modelled within the fracture gap. Thus, 32 total metatarsal geometry models were created to account for all parametric combinations of treatment and fracture type.

All models were imported into Abaqus (CAE 2019; Dassault Systèmes; Vélizy-Villacoublay, France) for subsequent meshing and FE analysis. The modeled orthopaedic hardware was meshed using 8-node linear hexahedral (C3D8R) elements, while the metatarsals were assigned 10-node quadratic tetrahedral (C3D10) elements to better accommodate the inherent geometric complexity of the bone (*Figure 3D*). All materials were assigned isotropic linear elastic material properties with exception to the cortical bone which was treated as transversely isotropic linear elastic (83). The material properties of the fracture callus were assumed to be spatially homogenous and the elastic modulus was parametrically varied to produce 17
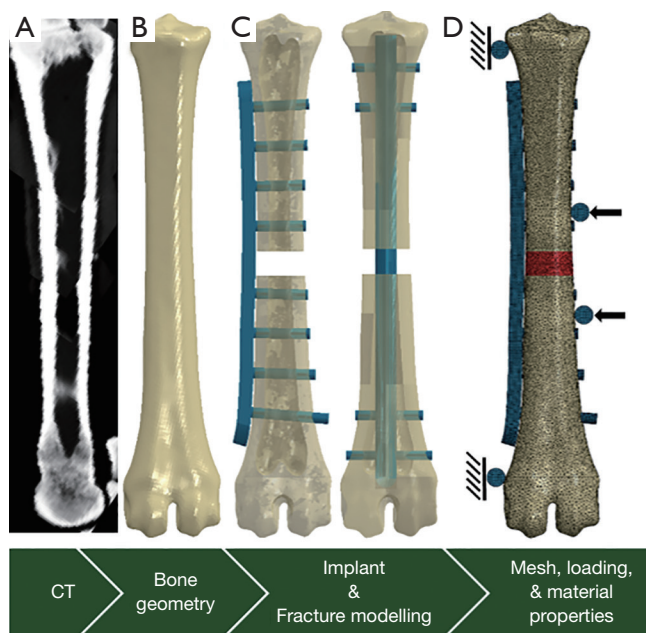
Figure 3 Methods of finite element (FE) analysis of fracture healing. (A) Computed tomography (CT) images were collected of an ovine metatarsal and (B) segmented into a three-dimensional model. (C) An osteotomy fracture was modeled and the bone fragments were stabilized by either locking compression plates (LCP) or intramedullary nails (IMN). (D) A mesh, of density determined via convergence study, was assigned and four-point bending loads were applied, as indicated by the black arrows, to produce 2 N-m maximum bending load. The type, material, and structure of fixation hardware (blue) was parametrically varied, as were the material properties and height of the osteotomy/endosteal callus (red). Deflection at the implant midspan nodes was measured for all models.

Table 1 Material properties assigned to finite element (FE) model

Material	Elastic modulus	Poisson ratio
Cortical bone	$^{\dagger}E_1 = 17.0$ GPa	$\nu_{12} = 0.48$
	$E_2 = 11.5$ GPa	$\nu_{23} = 0.40$
	$E_3 = 11.5$ GPa	$\nu_{31} = 0.48$
Stainless steel	$E = 193$ GPa	$\nu = 0.29$
Titanium	$E = 110$ GPa	$\nu = 0.34$
Callus	$^{\ddagger}E = $ [% of Cortical E_1]	$\nu = 0.30$
	$[1.0, 2.5, 5.0, 7.5] \times 10^{-2}$	
	$[1.0, 2.5, 5.0, 7.5] \times 10^{-1}$	
	$[1.0, 2.5, 5.0, 7.5] \times 10^{0}$	
	$[1.0, 2.5, 5.0, 7.5, 10] \times 10^{1}$	

†, subscripts denote the material direction, with 1 being longitudinal while 2 and 3 represent the orthotropic (transverse) directions (83); subscripts are omitted for materials modelled as isotropic. ‡, callus elastic modulus was parametrically increased, as a percentage of cortical bone, as an approximation of fracture healing.

values logarithmically spanning from 0.1% to 100% of cortical bone (*Table 1*). Implant fixation hardware was parametrically assigned material properties corresponding to SS or Ti. The effects of epiphyseal trabecular bone were assumed to be negligible based on the region of interest being the diaphyseal midspan and the epiphyses being located in regions of zero applied bending moment, thus trabecular bone was not included in these models.

To represent perfect screw fixation (i.e., no screw loosening), a tied constraint was applied at the interface between hardware members (i.e., locking screw heads to the LCP, or bolts to the IMN) and between bone and the fixation hardware (i.e., locking screw cortical threads or bolts to cortical bone). The loading and boundary conditions were assigned to match the *in vitro* four-point bending load used for DEC analysis (*Figure 3D*). To prevent rigid body translations, a zero proximal-distal-direction translation boundary condition was applied to the metatarsal proximal-distal mid-plane. Similarly, a zero cranial-caudal-direction translation boundary condition was applied to the metatarsal's cranial-caudal mid-plane.

The inner and outer contact points of four-point bending device were modeled as rigid cylinders of 6 mm diameter, and were symmetrically positioned such that the fracture site was centered between the contact points. Hard contact properties were assigned between the cylinder and cortical surfaces to facilitate application and transfer of mechanical load via these contact points. The outer bending points were assigned encastre boundary conditions while equal point loads were assigned to each of the inner bending points in order to produce a 2 N-m moment between the inner points. The primary data of interest for all models was the implant's midspan deflection, as measured by the displacement in the direction of applied load for nodes located at the implant midspan.

Mesh convergence study

A parametric mesh refinement study was performed to ensure that results were not influenced by inadequate mesh

Page 8 of 16

Wolynski et al. Healing bone fracture stiffness measured by diagnostic DEC

resolution. For both the LCP and IMN models, mesh convergence was performed using the parametric variation featuring 8 mm fracture, callus modulus of 0.01% of cortical bone, and standard hardware geometry. For the LCP model, four models with identical geometry and loading conditions were analyzed, with models being labeled Low (139,388 elements), Medium (239,195 elements), High (467,443 elements), and Extra High (773,909 elements). For all models, implant midspan deflection was predicted and total strain energy was calculated for the cortical bone, callus, and implant hardware regions of interest (ROI). Mesh refinement (i.e., reduction of the average element volume) beyond the High-density model caused implant deflection and strain energy in the callus and cortical bone to change by less than 4%. Further mesh refinement of the implant hardware in the High-density model caused the implant deflection and strain energy in all ROIs to change by less than 3%. This refined High density model (549,011 elements) was thus deemed to be fully converged.

Similar mesh convergence was performed in the IMN model with Low (84,505 elements), Medium (163,020 elements), High (318,626 elements), and Extra High (663,267 elements). Mesh refinement beyond the High-density model caused implant deflection and strain energy in the cortical bone and hardware to change by less than 4%. Further mesh refinement resulted in implant deflection and strain energy in all ROI to change by less than 3%; thus, this refined High-density model (382,909 elements) was deemed to be fully converged. The converged mesh resolutions from this sub-study were applied to all parametric analysis variations, although exact element counts varied slightly due to difference in model geometries.

Strain gage validation

To validate the accuracy of the FE models, strain results were compared between *in vitro* and *in silico* tests; strain, rather than implant deflection, was selected for the mechanical validation parameter to obviate measurement uncertainties associated with accurate observation of exceedingly small implant deflections (i.e., on the order of tens of μm). Cadaveric metatarsals (n=10) were obtained from animals sacrificed for unrelated studies, and all soft tissue was removed. All samples received a mid-diaphyseal ostectomy via bone saw, and half of the samples were stabilized via LCP while the others were stabilized via IMN. The hardware and fracture model were selected to recapitulate the parameters of the mesh validation

models. Following manufacturer recommended application techniques, stacked strain rosettes (C2A-06-062WW-350; Micro-Measurements; Raleigh, NC, USA) were adhered to the cortical bone between the two screws proximal to the fracture site (i.e., to avoid excessive strain gradients resulting from the screw holes of the LCP hardware), or to the IMN midspan. Samples were placed in a MT equipped with a four-point bending fixture of configuration mechanically comparable to the FE model loading conditions. Static four-point bending loads were applied (2.0 N-m, n=5 preload cycles from 0.0–3.0 N-m, and n=5 data collections per test) while maximum principal strain was measured using a custom data collection code (LabVIEW 2019; National Instruments; Austin, TX, USA).

Maximum principal strain from the two fully converged FE models were independently averaged from regions of comparable area to the strain rosettes (n=10 nodes and n=9 nodes for the LCP and IMN models, respectively). For both fixation methods, mean FE strain values (68.0±4.2 μϵ, 72.1±4.1 μϵ, for plate & IMN; respectively) were within one standard deviation of experimental strains (81.6±37.6 μϵ, 101.6±30.8 μϵ, for plate & IMN; respectively), thus the FE models were deemed validated.

Results

Ex vivo prediction of fracture stiffness

When quantifying fracture bending stiffness for progressively destabilized cadaveric fractures, no significant differences were observed for any fracture state for values obtained via MT methods versus DEC methods (P=0.587, P=0.985, P=0.975; for intact, DS, and FF comparisons; respectively; *Figure 4A*). Traditional MT techniques measured mean stiffness values (± standard deviation) of 19.6±5.8, 17.4±6.6, and 10.3±2.4 N-m/mm for the intact, DS, and FF states; respectively. Mean DEC stiffness predictions were not significantly different from the MT values, with values of 23.3±4.5, 18.9±9.0, and 11.9± 2.4 N-m/mm for the intact, DS, and FF, respectively. For each sample, percent differences between MT and DEC predictions of fracture stiffness were individually calculated for each fracture state; mean percent differences (± standard deviation, after outlier removal) were 22.7%±21.8%, 22.1%±15.6%, and 19.5%±12.1% for the intact, DS, and FF states; respectively (*Figure 4B*). DS and FF states each had single outliers, 95% and 75% respectively, which were not included in the preceding mean percent difference calculations. For both the MT and DEC techniques, mean
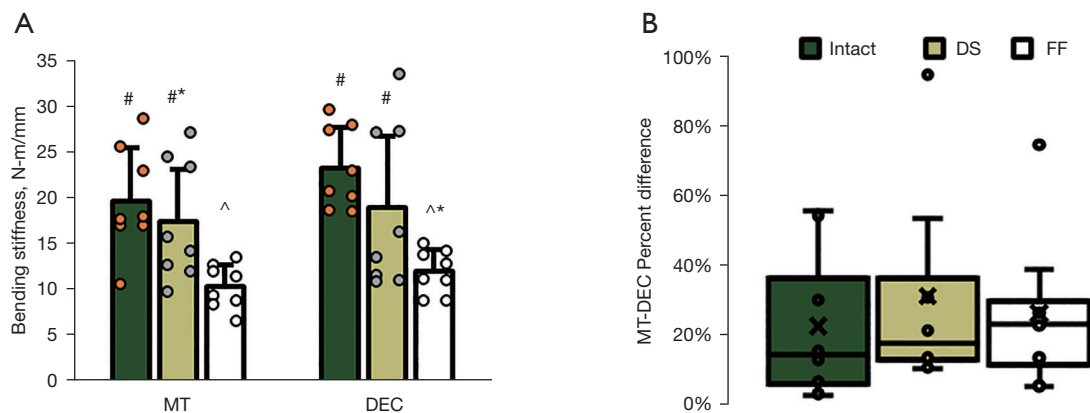
Figure 4 Fracture bending stiffness predictions. (A) Bending stiffness of cadaveric metatarsals of decreasing stability levels [i.e., intact, destabilized (DS), and fully fractured (FF) states] were measured using material testing (MT) methods and direct electromagnetic coupling (DEC) predictions. Bars depict mean + standard deviation, where overlaid points correspond to the mean values of each sample (n=8). Bars which do not share symbols (#, *, ^) are significantly different (P<0.05). (B) Percent differences of MT and DEC bending stiffness measurements for each sample (n=8) represented as a standard box and whisker plot.

stiffness values were significantly lower for the FF state than the intact (P<0.001 & P=0.002, respectively) and DS (P=0.030 & P=0.036, respectively) states. Calibrated DEC results, for an applied 2 N-m four-point bending load, predicted an 82.2 µm reduction in mean implant bending deflection from intact to FF states.

FE predictions of implant deflections

Parametric FE predictions of implant midspan deflections during four-point loading have been separated into individual semi-log charts according to the implant treatment type (*Figure 5*). The largest change in implant deflection (i.e., difference in implant deflections predicted at callus moduli of 0.01% and 100% of cortical bone) was 267.9 µm for the case of an 8 mm fracture treated via reduced stiffness Ti LCP (*Figure 5B*); however, the greatest individual instance of implant deflection, 316.0 µm, was observed at initial fracture (i.e., callus modulus =0.01% of cortical bone) for an 8 mm fracture treated via reduced stiffness Ti IMN (*Figure 5H*). The smallest predicted displacement was 24.43 µm and occurred at full healing (i.e., callus modulus =100%) for the 1 mm fracture stabilized by increased stiffness SS LCP (*Figure 5E*).

When fully healed, displacements for all fracture types within a given treatment permutation (i.e., callus modulus of 100% for all points within any individual plot of *Figure 5*) exhibited a set of values with standard deviations less than

0.5% of their mean, thus indicating convergence. At initial fracture, displacements for all fracture types within a given treatment permutation exhibited a set of values with standard deviations less than 7% of their mean. For the average stiffness SS model (i.e., comparable parameters to the fracture model used for *ex vivo* testing), mean implant displacement decreased by 74.7 µm from FF to fully healed states (*Figure 5C*).

Discussion

When destabilizing fractures, MT methods found significant differences in the bending stiffness of FF relative to DS and intact states. This supports the use of a progressive destabilization as a chronologically reversed approximation of fracture healing mechanics. DEC methods were similarly able to detect significant differences in FF stiffness relative to DS and intact states. Of primary interest to this study was the ability of DEC to accurately predict the magnitude of stiffness. For all fracture states, DEC predictions of fracture stiffness were not significantly different from values obtained by MT testing values (*Figure 4*).

While traditional MT methods are a gold-standard technique for quantifying structural properties in a laboratory setting, they are neither safe nor feasible for use as a clinical diagnostic tool. The data of this study, however, suggest DEC can predict fracture bending stiffness to within, on average, 23% difference of MT methods (*Figure 4B*),
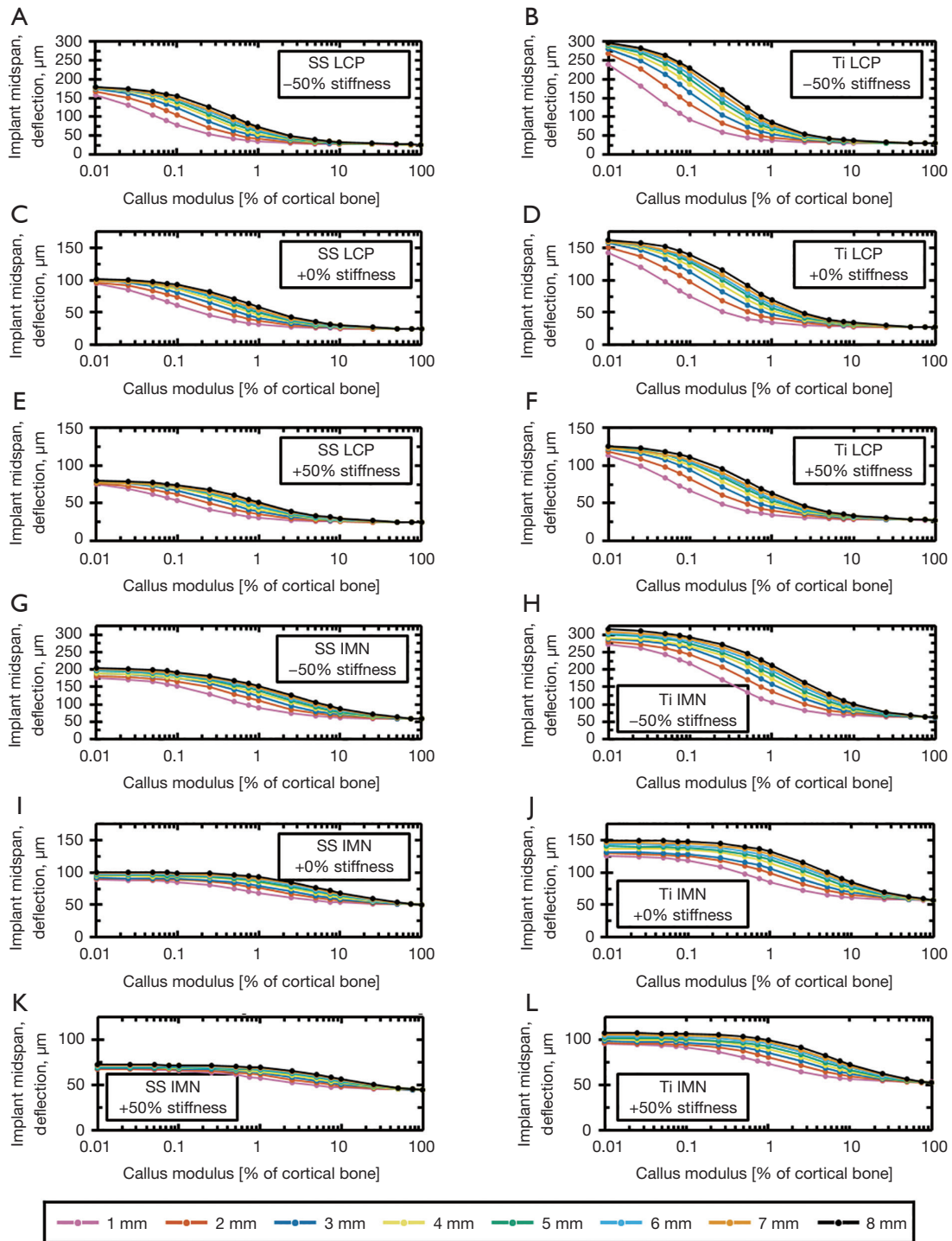
Figure 5 Parametric finite element (FE) predictions of implant deflections resulting from the application of experimentally equivalent four-point bending loads. Different colors correspond to the parametrically varied osteotomy fracture height. Each chart corresponds to a unique permutation of implant design: stainless steel [SS] or titanium [Ti] implant materials (charts A, C, E, G, I, & K or B, D, F, H, J, & L; respectively); locking compression plating (LCP) or intramedullary nailing (IMN) fixation (charts A-F or G-L, respectively); and implant design of 50% increased, 0% changed, or 50% reduced rigidity (according to bending direction second moment of area at the implant midspan; charts A-B & I-J; C-D & I-J; and E-F & K-L; respectively).

with no significant differences in values measured by each method for any fracture state (*Figure 4A*). Unlike MT devices, DEC is highly portable and non-invasive, and therefore well suited for use as a diagnostic tool in clinical or home tele-medicine applications. It should, however, be noted that individual samples did exhibit erroneously high percent differences in MT versus DEC predictions of fracture stiffness, thus suggesting that additional improvements are necessary to improve the reliability of this emerging technology.

The present results agree with previous DEC studies with regards to the ability of this technology to detect implant deflections (55) and differences in fracture stiffness (56,57). These studies showed success in using relative temporal changes in DEC antenna sensitivity to indicate the healing trajectory; however, the large antenna designs used in these early studies precluded the use of linear actuator antenna calibration procedures requisite for converting antenna sensitivity into fracture bending stiffness. The antenna sensitivity data provided by previous antenna versions are less clinically intuitive than fracture stiffness, and require continuous data to indicate relative changes in fracture stiffness. Thus, missed measurements during early healing, when using the previous antenna design, would potentially limit the predicative efficacy of DEC.

This study marks a substantial improvement in this technology due to the implementation of antenna calibration methods to accurately convert DEC measurements into fracture stiffness. Fracture stiffness is an absolute metric which can be obtained and interpreted at any point during the healing cascade, and provides an objective indication of healing status. It has been shown that human fracture stiffness magnitude of 15 N-m/degree is an effective benchmark to diagnose fracture union (21,33) and temporal changes in fracture stiffness can predict healing outcome 2.5 weeks prior to radiographic diagnosis (26). Thus, the demonstrable accuracy of DEC quantifications of fracture stiffness supports the conclusion that continued study and development of this technology may provide clinical utility for early prediction of fracture healing outcome.

The cadaveric simulations of this study exhibit compelling results for DEC as a diagnostic tool, but it should be noted that this fracture model implemented a simplified approximation of fracture healing for a single selection of fracture stabilization hardware. In a clinical setting, fracture healing progression is a continuous process and the permutations of fracture and treatment type are

innumerable. These studies also utilized an ovine cadaveric model, which have intrinsic structural differences in bone structure relative to humans. Additional *in vivo* large animal and preclinical fracture studies will therefore be pursued to better establish the efficacy of DEC in a clinical setting.

Despite these limitations, the mechanical behaviors necessary to DEC measurements were predicted for a large volume of fracture-treatment types using FE methods, hence obviating the need for excessive animal experimentation. Results of the current parametric FE study support the foundational hypothesis that implant deflections during four-point bending decrease in accordance with healing induced increases in callus bending rigidity. FE and DEC cadaveric simulations of comparable fracture fixation models aligned closely, with total predicted implant bending deflection reduction (FF to fully intact states) agreeing within 10% (74.7 and 82.2 µm, respectively).

For all permutations of fracture and treatment type, FE implant displacement predictions decreased non-linearly with increasing callus elastic modulus (*Figure 5*). These results agree with the findings of Richardson *et al.* (21) which, in human clinical tibia fracture treated via external fixation, found fracture stiffness to non-linearly increase over time. This temporal stiffness profile was characterized by exponential increase during the early stages of healing, followed by a plateau upon reaching the stiffness of an intact tibia. The results of this clinical study agree closely with the profiles observed in *Figure 5*, assuming an inverse relationship between implant deflection and fracture stiffness.

All FE fracture models for a given fracture type featured similar implant displacements at initial fracture, and converged to a common displacement at fully healed states, but paths between these two points varied considerably (*Figure 5*). Small fracture gaps exhibited rapid reductions in implant deflections for small increases in callus modulus, while increasing fracture gap size delayed this reduction. This effect became increasingly pronounced with decreasing stiffness of fracture fixation hardware (i.e., using Ti versus SS, or implant structures of −50% versus +50% inherent stiffness). These findings suggest that the total magnitude of implant deflection/stiffness changes throughout proper healing, as measured via DEC, is influenced exclusively by fixation implant type and callus mechanics, and is irrespective of fracture size. However, it should be noted that this observation neglects the effects of fracture size on callus formation in a clinical setting (i.e., not all callus will present with the structural and material homogeneity

assumed in this study).

In all cases, increases in hardware stiffness decreased the total change in implant deflections throughout the healing duration. Implant deflections are foundational to DEC predictions of fracture stiffness; thus, these data suggest that DEC is especially well suited for cases with less rigid fracture fixation. For example, fractures with increased stiffness SS IMN fixation exhibit relatively low change in deflections (*Figure 5K*), therefore repeated DEC measurements can be expected to be exhibit similar temporal stiffness for fractures trending towards union (i.e., callus elastic modulus increasing) and for fractures trending towards adverse healing (i.e., callus elastic modulus is invariant). Conversely, properly healing fractures treated by Ti LCP fixation exhibit large implant deflection reductions during the early stages of healing (*Figure 5B*), and therefore will provide clear differences in temporal stiffness profiles of fractures trending towards proper union (i.e., stiffness progressively increases) and those trending towards adverse healing (i.e., stiffness is invariant).

Significant differences in DEC fracture stiffness were observed between the intact and FF states, suggesting that changes in implant deflections exceeding 82.2 μm (i.e., total predicted implant deflection reduction using calibrated DEC) can be confidently detected for indicating healing state. FE results indicate average total deflection reductions to be approximately equal to (within 10%) or exceeding this benchmark for all but the most rigid implant designs (53.5, 44.4, 48.5, 25.2 μm; for models of increased stiffness SS LCP, mean stiffness SS IMN, increased stiffness Ti IMN, and increased stiffness SS IMN; respectively). *Ex vivo* experiments of the current study were not designed to specifically elucidate the minimum deflection resolution of the DEC antenna, therefore future studies will be conducted to better characterize the efficacy of DEC for these highly rigid treatment types.

As with the cadaveric study, this FE analysis is somewhat limited by its simplistic approximation of fracture healing. Modeled fracture types were limited to mid-diaphyseal transverse fractures, and callus was assumed to be of index 1.0 (i.e., no periosteal callus formation) with spatially homogeneous material properties. In a clinical setting, fracture healing is more complex with inhomogeneous material and structural modifications in response to the mechanical environment of the fracture site (6). While advanced FE models of fracture healing can implement such analysis (84,85), it was deemed unnecessary for this study as any callus of inhomogeneous structure/composition will feature an overall structural rigidity comparable to some point within the range of materials tested in this study (i.e., the rigidity falls some point between the 0.01% and 100% callus models tested herein).

It is important to clarify that the dependent variable presented in *Figure 5* is callus elastic modulus, which does not directly correspond to healing time. Clinical fracture healing is a highly variable process, thus mapping callus modulus to healing time cannot be done with any level of confidence, especially when considering that increased fracture gaps are known to exhibit delayed healing (6).

This cadaveric study is not a perfect representation of clinical fracture healing, but provides a reasonable approximation of what can be expected of DEC at the extrema of the fracture healing cascade (i.e., FF and fully healed), and FE results further bolster the validity of the mechanics foundational to DEC for a large volume/variety of fracture and hardware stabilization types. The results of the current study indicate that the novel Vivaldi antenna style DEC antenna exhibits the same diagnostic traits of previous coiled-coaxial cable designs, yet with a smaller antenna profile and increased sensing resolution. Additionally, the calibration methods presented provide a means to accurately quantify fracture stiffness, thus marking a pivotal step forward for the clinical translatability of this technology.

The small antenna footprint and its demonstrated accuracy in quantifying objective metrics of fracture healing provide a path to utility in clinical and/or home tele-medicine settings, where it will augment radiographic imaging to improve the time and confidence of adverse healing diagnoses. Thus, the results of these experiments warrant additional studies of this technology, to better characterize the efficacy of this novel diagnostic tool in a clinically translatable fracture model.

Acknowledgments

Footnote

Reporting Checklist: The authors have completed the ARRIVE reporting checklist. Available at https://atm.

amegroups.com/article/view/10.21037/atm-21-5315/rc

Data Sharing Statement: Available at https://atm.amegroups.com/article/view/10.21037/atm-21-5315/dss

Peer Review File: Available at https://atm.amegroups.com/article/view/10.21037/atm-21-5315/prf

Conflicts of Interest: All authors have completed the ICMJE uniform disclosure form (available at https://atm.amegroups.com/article/view/10.21037/atm-21-5315/coif). Funding for this project was supported by the NIH-NIAMS. Additional funding from the NIH and Colorado Office of Economic Development and International Trade (COEDIT) supported related research, but did not directly support this presented work. JGW and Drs. KML, CMP, and KCM are authors of pending and issued patents related to the DEC technology presented in this manuscript. The authors have no other conflicts of interest to declare.

Ethical Statement: The authors are accountable for all aspects of the work in ensuring that questions related to the accuracy or integrity of any part of the work are appropriately investigated and resolved. Ethical committee approval was not required because cadaveric animal tissues used in this study were harvested from animals sacrificed for reasons unrelated to this study.

Open Access Statement: This is an Open Access article distributed in accordance with the Creative Commons Attribution-NonCommercial-NoDerivs 4.0 International License (CC BY-NC-ND 4.0), which permits the non-commercial replication and distribution of the article with the strict proviso that no changes or edits are made and the original work is properly cited (including links to both the formal publication through the relevant DOI and the license). See: https://creativecommons.org/licenses/by-nc-nd/4.0/.

References

1. Antonova E, Le TK, Burge R, et al. Tibia shaft fractures: costly burden of nonunions. BMC Musculoskelet Disord 2013;14:42.
2. Brinker MR, Hanus BD, Sen M, et al. The devastating effects of tibial nonunion on health-related quality of life. J Bone Joint Surg Am 2013;95:2170-6.
3. Kanakaris NK, Giannoudis PV. The health economics of the treatment of long-bone non-unions. Injury 2007;38 Suppl 2:S77-84.
4. Heckman JD, Sarasohn-Kahn J. The economics of treating tibia fractures. The cost of delayed unions. Bull Hosp Jt Dis 1997;56:63-72.
5. Oryan A, Monazzah S, Bigham-Sadegh A. Bone injury and fracture healing biology. Biomed Environ Sci 2015;28:57-71.
6. Claes LE, Heigele CA, Neidlinger-Wilke C, et al. Effects of mechanical factors on the fracture healing process. Clin Orthop Relat Res 1998;(355 Suppl):S132-47.
7. Claes L, Recknagel S, Ignatius A. Fracture healing under healthy and inflammatory conditions. Nat Rev Rheumatol 2012;8:133-43.
8. Jagodzinski M, Krettek C. Effect of mechanical stability on fracture healing--an update. Injury 2007;38 Suppl 1:S3-10.
9. Giannoudis PV, Kanakaris NK. Non-unions. In: Lasanianos NG, Kanakaris NK, Giannoudis PV, editors. Trauma and Orthopaedic Classifications: A Comprehensive Overview. London: Springer London, 2015:529-32.
10. Mills L, Tsang J, Hopper G, et al. The multifactorial aetiology of fracture nonunion and the importance of searching for latent infection. Bone Joint Res 2016;5:512-9.
11. Calori GM, Albisetti W, Agus A, et al. Risk factors contributing to fracture non-unions. Injury 2007;38 Suppl 2:S11-8.
12. Gaston MS, Simpson AH. Inhibition of fracture healing. J Bone Joint Surg Br 2007;89:1553-60.
13. Santolini E, West R, Giannoudis PV. Risk factors for long bone fracture non-union: a stratification approach based on the level of the existing scientific evidence. Injury 2015;46 Suppl 8:S8-S19.
14. Blokhuis TJ, de Bruine JH, Bramer JA, et al. The reliability of plain radiography in experimental fracture healing. Skeletal Radiol 2001;30:151-6.
15. Hammer RR, Hammerby S, Lindholm B. Accuracy of radiologic assessment of tibial shaft fracture union in humans. Clin Orthop Relat Res 1985;(199):233-8.
16. Whelan DB, Bhandari M, McKee MD, et al. Interobserver and intraobserver variation in the assessment of the healing of tibial fractures after intramedullary fixation. J Bone Joint Surg Br 2002;84:15-8.
17. McClelland D, Thomas PB, Bancroft G, et al. Fracture healing assessment comparing stiffness measurements using radiographs. Clin Orthop Relat Res 2007;457:214-9.
18. Davis BJ, Roberts PJ, Moorcroft CI, et al. Reliability of radiographs in defining union of internally fixed fractures.

Page 14 of 16

Wolynski et al. Healing bone fracture stiffness measured by diagnostic DEC

Injury 2004;35:557-61.

19. Bhandari M, Guyatt GH, Swiontkowski MF, et al. A lack of consensus in the assessment of fracture healing among orthopaedic surgeons. J Orthop Trauma 2002;16:562-6.

20. Marsh D. Concepts of fracture union, delayed union, and nonunion. Clin Orthop Relat Res 1998;(355 Suppl):S22-30.

21. Richardson JB, Cunningham JL, Goodship AE, et al. Measuring stiffness can define healing of tibial fractures. J Bone Joint Surg Br 1994;76:389-94.

22. Joslin CC, Eastaugh-Waring SJ, Hardy JR, et al. Weight bearing after tibial fracture as a guide to healing. Clin Biomech (Bristol, Avon) 2008;23:329-33.

23. Claes LE, Cunningham JL. Monitoring the mechanical properties of healing bone. Clin Orthop Relat Res 2009;467:1964-71.

24. Wehner T, Gruchenberg K, Bindl R, et al. Temporal delimitation of the healing phases via monitoring of fracture callus stiffness in rats. J Orthop Res 2014;32:1589-95.

25. Wade RH, Moorcroft CI, Thomas PB. Fracture stiffness as a guide to the management of tibial fractures. J Bone Joint Surg Br 2001;83:533-5.

26. Claes L, Grass R, Schmickal T, et al. Monitoring and healing analysis of 100 tibial shaft fractures. Langenbecks Arch Surg 2002;387:146-52.

27. Hente R, Cordey J, Perren SM. In vivo measurement of bending stiffness in fracture healing. Biomed Eng Online 2003;2:8.

28. Webb J, Herling G, Gardner T, et al. Manual assessment of fracture stiffness. Injury 1996;27:319-20.

29. Amin S, Achenbach SJ, Atkinson EJ, et al. Trends in fracture incidence: a population-based study over 20 years. J Bone Miner Res 2014;29:581-9.

30. Stoffel K, Klaue K, Perren SM. Functional load of plates in fracture fixation in vivo and its correlate in bone healing. Injury 2000;31 Suppl 2:S-B37-50.

31. Kienast B, Kowald B, Seide K, et al. An electronically instrumented internal fixator for the assessment of bone healing. Bone Joint Res 2016;5:191-7.

32. McGilvray KC, Unal E, Troyer KL, et al. Implantable microelectromechanical sensors for diagnostic monitoring and post-surgical prediction of bone fracture healing. J Orthop Res 2015;33:1439-46.

33. Dwyer JS, Owen PJ, Evans GA, et al. Stiffness measurements to assess healing during leg lengthening. A preliminary report. J Bone Joint Surg Br 1996;78:286-9.

34. Schmickal T, von Recum J, Wentzensen A. Stiffness measurement of the neocallus with the Fraktometer FM 100. Arch Orthop Trauma Surg 2005;125:653-9.

35. Seide K, Weinrich N, Wenzl ME, et al. Three-dimensional load measurements in an external fixator. J Biomech 2004;37:1361-9.

36. Grasa J, Gómez-Benito MJ, González-Torres LA, et al. Monitoring in vivo load transmission through an external fixator. Ann Biomed Eng 2010;38:605-12.

37. Ogrodnik PJ, Moorcroft CI, Thomas PB. Measuring multi-dimensional, time-dependent mechanical properties of a human tibial fracture using an automated system. Proc Inst Mech Eng H 2007;221:641-52.

38. Wolynski JG, Sutherland CJ, Demir HV, et al. Utilizing Multiple BioMEMS Sensors to Monitor Orthopaedic Strain and Predict Bone Fracture Healing. J Orthop Res 2019;37:1873-80.

39. Wilson DJ, Morgan RL, Hesselden KL, et al. A single-channel telemetric intramedullary nail for in vivo measurement of fracture healing. J Orthop Trauma 2009;23:702-9.

40. Seide K, Aljudaibi M, Weinrich N, et al. Telemetric assessment of bone healing with an instrumented internal fixator: a preliminary study. J Bone Joint Surg Br 2012;94:398-404.

41. Schneider E, Michel MC, Genge M, et al. Loads acting in an intramedullary nail during fracture healing in the human femur. J Biomech 2001;34:849-57.

42. Fischer WJ, Sauer S, Marschner U, et al. Galfenol resonant sensor for indirect wireless osteosynthesis plate bending measurements. Proc. IEEE Sens. Conf.; 2009 2009; Christchurch, Canterbury, New Zealand: IEEE.

43. Oess NP, Weisse B, Nelson BJ. Magnetoelastic Strain Sensor for Optimized Assessment of Bone Fracture Fixation. IEEE Sens J 2009;9:961-8.

44. Sauer S, Marschner U, Adolphi B, et al. Passive Wireless Resonant Galfenol Sensor for Osteosynthesis Plate Bending Measurement. IEEE Sens J 2012;12:1226-33.

45. Tan Y, Hu J, Ren L, et al. A Passive and Wireless Sensor for Bone Plate Strain Monitoring. Sensors (Basel) 2017;17:2635.

46. Wachs RA, Ellstein D, Drazan J, et al. Elementary Implantable Force Sensor: For Smart Orthopaedic Implants. Adv Biosens Bioelectron 2013.

47. Melik R, Perkgoz NK, Unal E, et al. Bio-implantable passive on-chip RF-MEMS strain sensing resonators for orthopaedic applications. J Micromech Microeng 2008;18.

48. Melik R, Unal E, Kosku Perkgoz N, et al. Flexible metamaterials for wireless strain sensing. Appl Phys Lett

2009;95:181105.

49. Melik R, Unal E, Perkgoz NK, et al. Circular High-Q Resonating Isotropic Strain Sensors with Large Shift of Resonance Frequency under Stress. Sensors (Basel) 2009;9:9444-51.

50. Melik R, Unal E, Perkgoz NK, et al. Metamaterial-based wireless strain sensors. Appl Phys Lett 2009;95:011106.

51. Melik R, Unal E, Perkgoz NK, et al. Metamaterial based telemetric strain sensing in different materials. Opt Express 2010;18:5000-7.

52. Melik R, Unal E, Perkgoz NK, et al. Metamaterial-based wireless RF-MEMS strain sensors. 2010 IEEE Sensors; 2010. Available online: https://ieeexplore.ieee.org/document/5690582

53. Melik R, Unal E, Perkgoz NK, et al. RF-MEMS Load Sensors with Enhanced Q-factor and Sensitivity in a Suspended Architecture. Microelectron Eng 2011;88:247-53.

54. Melik R, Unal E, Perkgoz NK, et al. Nested Metamaterials for Wireless Strain Sensing. IEEE J Sel Top Quantum Electron 2010;16:450-8.

55. Labus KM, Notaros BM, Ilic MM, et al. A Coaxial Dipole Antenna for Passively Sensing Object Displacement and Deflection for Orthopaedic Applications. IEEE Access 2018;6:68184-94.

56. Labus KM, Sutherland C, Notaros BM, et al. Direct electromagnetic coupling for non-invasive measurements of stability in simulated fracture healing. J Orthop Res 2019;37:1164-71.

57. Wolynski JG, Labus KM, Easley JT, et al. Diagnostic prediction of ovine fracture healing outcomes via a novel multi-location direct electromagnetic coupling antenna. Ann Transl Med 2021;9:1223.

58. Wolynski JG, Ilić MM, Notaroš BM, et al. A Vivaldi Antenna for Passively Sensing Object Deflection for Orthopaedic Applications. Available online: https://ieeexplore.ieee.org/stamp/stamp.jsp?arnumber=9661431

59. Steiner M, Claes L, Ignatius A, et al. Numerical simulation of callus healing for optimization of fracture fixation stiffness. PLoS One 2014;9:e101370.

60. Ganesh VK, Ramakrishna K, Ghista DN. Biomechanics of bone-fracture fixation by stiffness-graded plates in comparison with stainless-steel plates. Biomed Eng Online 2005;4:46.

61. Gómez-Benito MJ, García-Aznar JM, Kuiper JH, et al. A 3D computational simulation of fracture callus formation: influence of the stiffness of the external fixator. J Biomech Eng 2006;128:290-9.

62. Wee H, Reid JS, Chinchilli VM, et al. Finite Element-Derived Surrogate Models of Locked Plate Fracture Fixation Biomechanics. Ann Biomed Eng 2017;45:668-80.

63. Cao Y, Zhang Y, Huang L, et al. The impact of plate length, fibula integrity and plate placement on tibial shaft fixation stability: a finite element study. J Orthop Surg Res 2019;14:52.

64. Favre P, Kloen P, Helfet DL, et al. Superior versus anteroinferior plating of the clavicle: a finite element study. J Orthop Trauma 2011;25:661-5.

65. Stoffel K, Dieter U, Stachowiak G, et al. Biomechanical testing of the LCP--how can stability in locked internal fixators be controlled? Injury 2003;34 Suppl 2:B11-9.

66. Zhao X, Li J, Chen Y, et al. Investigation of load transfer process between external fixator and bone model by experimental and finite element methods. J Appl Biomater Funct Mater 2019;17:2280800019826512.

67. Li J, Zhao X, Hu X, et al. A theoretical analysis and finite element simulation of fixator-bone system stiffness on healing progression. J Appl Biomater Funct Mater 2018;16:115-25.

68. Li J, Zhao X, Hu X, et al. A finite element analysis for monitoring the healing progression of fixator-bone system under three loading conditions. Biomed Mater Eng 2018;29:473-83.

69. Zhang YK, Wei HW, Lin KP, et al. Biomechanical effect of the configuration of screw hole style on locking plate fixation in proximal humerus fracture with a simulated gap: A finite element analysis. Injury 2016;47:1191-5.

70. Ghiasi MS, Chen JE, Rodriguez EK, et al. Computational modeling of human bone fracture healing affected by different conditions of initial healing stage. BMC Musculoskelet Disord 2019;20:562.

71. Gómez-Benito MJ, García-Aznar JM, Kuiper JH, et al. Influence of fracture gap size on the pattern of long bone healing: a computational study. J Theor Biol 2005;235:105-19.

72. Miramini S, Zhang L, Richardson M, et al. Influence of fracture geometry on bone healing under locking plate fixations: A comparison between oblique and transverse tibial fractures. Med Eng Phys 2016;38:1100-8.

73. Oh JK, Sahu D, Ahn YH, et al. Effect of fracture gap on stability of compression plate fixation: a finite element study. J Orthop Res 2010;28:462-7.

74. Lacroix D, Prendergast PJ. A mechano-regulation model for tissue differentiation during fracture healing: analysis of gap size and loading. J Biomech 2002;35:1163-71.

75. Andreykiv A, van Keulen F, Prendergast PJ. Simulation of

fracture healing incorporating mechanoregulation of tissue differentiation and dispersal/proliferation of cells. Biomech Model Mechanobiol 2008;7:443-61.

76. García-Aznar JM, Kuiper JH, Gómez-Benito MJ, et al. Computational simulation of fracture healing: influence of interfragmentary movement on the callus growth. J Biomech 2007;40:1467-76.

77. Lipphaus A, Witzel U. Finite-Element Syntheses of Callus and Bone Remodeling: Biomechanical Study of Fracture Healing in Long Bones. Anat Rec (Hoboken) 2018;301:2112-21.

78. Steiner M, Claes L, Ignatius A, et al. Disadvantages of interfragmentary shear on fracture healing--mechanical insights through numerical simulation. J Orthop Res 2014;32:865-72.

79. Wehner T, Steiner M, Ignatius A, et al. Prediction of the time course of callus stiffness as a function of mechanical parameters in experimental rat fracture healing studies--a numerical study. PLoS One 2014;9:e115695.

80. Pearce AI, Richards RG, Milz S, et al. Animal models for implant biomaterial research in bone: a review. Eur Cell Mater 2007;13:1-10.

81. Martini L, Fini M, Giavaresi G, et al. Sheep model in orthopedic research: a literature review. Comp Med 2001;51:292-9.

82. Yushkevich PA, Piven J, Hazlett HC, et al. User-guided 3D active contour segmentation of anatomical structures: significantly improved efficiency and reliability. Neuroimage 2006;31:1116-28.

83. Reilly DT, Burstein AH. The elastic and ultimate properties of compact bone tissue. J Biomech 1975;8:393-405.

84. de Alcântara ACS, Assis I, Prada D, et al. Patient-Specific Bone Multiscale Modelling, Fracture Simulation and Risk Analysis-A Survey. Materials (Basel) 2019;13:106.

85. Kim HJ, Chang SH, Jung HJ. The simulation of tissue differentiation at a fracture gap using a mechano-regulation theory dealing with deviatoric strains in the presence of a composite bone plate. Compos B Eng 2012;43:978-87.